Improved laser induced damage thresholds of Ar ion implanted fused silica at different ion fluences

Bo Li[a,b], Xia Xiang[a,*], Wei Liao[b,*], Shaobo Han[a], Jingxia Yu[a], Xiaolong Jiang[b], Haijun Wang[b], Muhammad Mushtaq[a], Xiaodong Yuan[b], Xiaotao Zu[a], and Yongqing Fu[c]

[a] School of Physics, University of Electronic Science and Technology of China, Chengdu 610054, China

[b] Research Center of Laser Fusion, China Academy of Engineering Physics, Mianyang 621900, China

c Faculty of Engineering and Environment, Northumbria University, Newcastle upon Tyne, NE1 8ST, UK

Abstract: In this work, effects of 10 keV argon ion implantation on laser-induced damage threshold (LIDT) of fused silica were systematically investigated with ion fluences ranged from 1×10^{16} ions/cm^2 to 1×10^{18} ions/cm^2. Results show that only when the ion fluence increases above 1×10^{17} ions/cm^2, the surface roughness apparently increases due to the formation of argon bubbles in the surface of fused silica. The concentration of defects decreases with the increased fluences up to 1×10^{17} ions/cm^2 but then increases further, especially for the oxygen deficient center (ODC) defect. Based on the nanoindentation test results, Ar ion implantation generates large compressive stress and strengthens the surface of fused silica by surface densification. With the increase of the Ar ion fluences, the LIDTs of the samples increase due to the increases in both surface compressive stress and defects annihilation. However, at higher ion fluences, the increase of the densities of defects and argon bubbles are identified as the key reasons for the decrease of the LIDTs. Therefore, Ar ion implantation can improve the LIDTs of fused silica at moderate fluences.

Keywords: Fused silica; ion implantation; surface morphology; optical property; compressive stress; laser damage threshold

1. Introduction

* Corresponding authors.

E-mail addresses: xiaxiang@uestc.edu.cn (X. Xiang), benleo4job@163.com (W. Liao).

Because of its excellent optical, thermal and mechanical properties, fused silica is one of the important optical materials widely used as transparency optics for high power laser systems[1-3]. However, laser induced damage leads to performance degradation of fused silica optics, and seriously reduces the lifetime of the optics and the load capacity of the high power laser facilities. In particular, 3ω optical damage is an important design constraint for the laser systems operated with high fluences [4]. Hence, it has been one of the major focuses in research on how to improve damage resistance and lifetime of fused silica optics in the past decades. The methods such as wet chemical etching, plasma and ion beam etching, UV and CO_2 laser treatments [5-8] have been reported to effectively improve the laser-induced damage threshold (LIDT) of the fused silica optics. However, the LIDT value of the fused silica surface is still much lower than the dielectric breakdown threshold of the bulk material mainly due to the surface and subsurface defects. Further research has been focused on removal of surface residual polishing powders, passivation or elimination of sub-surface defects, passivation and smoothening of damage craters, and improvement of surface quality, etc.

However, up to now, the effect of mechanical properties of the silica material such as stress-state on the laser damage resistance of fused silica has not been seriously considered to further improve the LIDT.

Dahmani et al. utilized the aluminum aperture to carry out the mechanical loading on the surrounding of the fused silica optics, and found that the uniform compressive stress of -6 psi loading on the component surface can effectively improve initial damage threshold and restrain the crack propagation, and accordingly, the LIDT for the 351 nm laser has been increased by 70% [9]. Kusov et al. developed a thermo-elastic model for laser-induced damage in metals and dielectrics, which predicted that the compressive stress can enhance the LIDT of the materials [10]. Thus, applying compressive stress on the fused silica surface can reduce the damage probability and growth of the optical components. Unfortunately the commonly used methods to create compressional layers and therefore strengthen conventional glass cannot be directly applied to fused silica. For example, these methods include the physical methods of surface melting and rapid quenching， and the chemical methods such as ionic exchange reactions with molten potassium nitrate. Silica sublimes rapidly near its melt temperature and contains no ions to exchange, thwarting these physical and chemical methods, respectively [11]. Ion beam bombardment can lead to the compressive stress formed on the material surface resulted from surface densification, defect formation and structural change, and the amplitude of stress can be adjusted by ion beam

parameters [12, 13]. Therefore, ion beam modification offers an opportunity for altering the stress-state of fused silica surface to mitigate the laser induced damage. Popman et al. have studied the mechanism and the effects of energetic heavy ions on the stress-state of fused silica using 4 MeV xenon ions [12, 14]. Felter et al. investigated heavy ion implantation in MeV energy range into bulk silica and their subsequent responses to high intensity ultra violet light. The results showed that there are no apparent changes in laser damage threshold of fused silica despite clear alteration of the stress-state in the glass. They also proposed that proper implantation conditions may reduce the defects, increase compressive stress in surface, and improve optical characteristics [11]. Up to now, little work has been done to investigate the influence of the stress induced by ion implantation on the laser damage behavior of fused silica. In addition, there is also interest to study the effects of ion implantation on the surface morphology and optical properties of the fused silica.

In this work, 10 keV argon ions were implanted into fused silica at various fluences ranged from 1×10^{16} ions/cm^2 to 1×10^{18} ions/cm^2. Surface morphology, optical and mechanical properties, laser-induced damage threshold were investigated. The results are helpful to understand the laser damage behavior of fused silica after Ar ion implantation and to optimize process parameters to improve the laser-induced damage threshold of the fused silica optics.

2. Experimental

Fused silica (Corning 7980, 30×30×4mm^3) were all ground and polished by the same vendor, with similar surface qualities, to ensure the comparison of test data. Before ion implantation, all the samples were firstly etched for 10 min in a buffered hydrofluoric acid solution (BHF, 1%HF+15%NH_4F+84%H_2O) in order to remove the surface contamination, re-deposited layer and blunt the subsurface defects. Then the samples were cleaned immediately with highly pure water and were dehydrated with alcohol. In this way, we can ensure that the stress formed by the ion implantation becomes the main factor to determine the LIDT of the optical component.

The prepared samples were implanted with 10 keV Ar ions at different fluences of 1×10^{16}, 5×10^{16}, 1×10^{17}, 5×10^{17}, and 1×10^{18} ions/cm^2 in a chamber with a base vacuum of 2×10^{-3} Pa. The ion beam current density was controlled at 53 μA/cm^2 so that Ar ions were implanted into fused silica samples in a relatively short time (30 seconds to 50 minutes) to reduce environmental pollution of the samples. In order to understand the etching rate, the profilometer measurement was applied. The etching rate of Ar ions to the sample at this beam

current density was ~2.05 nm/min, so the sputtering effect could be neglected at low fluence. But it needs to be considered at highest fluence indeed. The sample stage was kept at room temperature by the circulation of cooling water during the implantation process.

The projected range and the damage level induced by the Ar ions were simulated by SRIM 2008 code [15] and TRIDYN 2017 code, respectively. A cross sectional transmission electron microscopic (TEM) image was obtained by a Cs-corrector FEI Titan microscope operating at 300 kV. Before and after the ion implantation, surface morphologies of samples were characterized using a Nikon ECLIPSE LV100 optical microscope and a PSIA XE-100 atomic force microscope (AFM). Photoluminescence (PL) spectra were obtained using a Perkin-Elmer LS55 fluorescence spectrometer, with a gated photomultiplier used as a detector and a 20 W Xe discharge lamp for 8 μs duration used as an excitation source. The excitation wavelength was 240 nm (i.e., 5.16 eV) and the slit width for exciting and emission are 15 nm and 20 nm, respectively. Fourier transform infrared spectra (FTIR) were measured using a Nicolet 5700 spectrometer with an attenuated total reflection mode. The measurements were carried out in a range of 550 cm^{-1}-1500 cm^{-1}, with 32 scans and a resolution of 0.5 cm^{-1}. Tests on the mechanical characteristics of ion-implanted and un-implanted samples were performed using a nanoindentation tester (NHT^2 from Anton Parr) with a Berkovich indenter. The multiple loading/unloading indentation force and the corresponding displacement depth as the indenter penetrates into the specimen were recorded for each indentation. Then the load-depth curves were obtained to calculate the residual stress, hardness and elastic modulus of the modified surfaces. All the characterizations were carried out at room temperature.

The LIDT tests were performed on the exit surfaces of un-implanted and ion-implanted samples using a mono-longitudinal mode Nd:YAG laser operated at 355 nm with a pulse width of 6.3 ns. The spatial beam profile was near Gaussian distribution with a beam area of 0.8 mm^2 at $1/e^2$. The damage threshold was tested with R-on-1 procedure [16], in which the damage threshold was defined by irradiating the same area with a number of pulses at a repetition frequency with an increasing laser energy until the damage occurred. Damage was defined when a visible modification of sample surface was detected with CCD camera. An EMP 1000 energy meter was used to collect the energy data of each shot for calculating the value of the LIDT.

3. Results and Discussions

3.1. Ar ion distribution and Displacement damage estimate

SRIM 2008 code and TRIDYN 2017 code were utilized to calculate the range of Ar ions and the amount of displacement damage for 10 keV Ar ions implanted into fused silica with various fluences. The simulated parameters are listed in Table 1. Fig. 1(a) shows the depth distributions of Ar ions at different fluences from the SRIM simulation. TRIM assumes a uniform and unchanged fused silica substrate during the implantation process, which results in a depth profile that is close to a Gaussian distribution. The peak positions of Ar ion distribution in fused silica are the same at the depth of 13 nm under different ion fluences. The concentration of Ar ions increases with the increasing ion fluence, but the depth of ion implantation remains same and the value is approximately 40 nm. In contrast, the TRIDYN simulation considers the dynamic changes of the target during the ion implantation process. Then the depth distributions of Ar ions simulated by TRIDYN are shown in Fig. 1(b). The depth profiles of Ar ions implanted into fused silica are consistent with the results calculated by SRIM at low fluences. For the high fluences, the depth profiles shift towards the surface indicating the significant contribution from sputtering, which is consistent with the etching rate measured by the profilometer. The concentration of Ar ions also increases with the increasing fluence and then gradually tends to saturation when the fluence exceeds 1×10^{17} ions/cm^2. Compared with the SRIM simulation, TRIDYN predicts a lower concentration of Ar ions in the depth profile due to continued surface sputtering during the implantation process that removes the fused silica surface with the already implanted Ar ions at higher fluences. Because of the diffusion of implanted ions, the depth of Ar ion distribution (~50 nm) is larger than the results calculated by SRIM, which is linked with the depth of the stress distribution.

The displacement per atom (dpa) is introduced to show the damage level when the ions interact with the materials. Fig. 1(c) shows the depth distributions of dpa in the fused silica calculated by SRIM. As the ion fluence increases, the displacement damage of the irradiated sample becomes significant. The ion implantation will damage the fused silica and induce defects such as E' color centers and other lattice defects, and even Ar bubbles if the ion fluence is very large [17]. Fig. 1(d) shows the depth distributions of dpa simulated by TRIDYN. The dpa increases with the increasing fluence and then gradually trends to saturation. Because of ion implantation into fused silica accompanied by sputtering on the surface, the depth profile of dpa has significantly shifted towards the surface resulting in the displacement damage generating on the surface of the sample and decreasing exponentially with the increasing depth. The total thickness of the damage layer is corresponding to the depth of Ar ion distribution.

Generally, TRIDYN code takes into account the specific processes such as sputtering, swelling and diffusion. These processes will result in shifting the depth profile toward the surface, decreasing the concentration of Ar ions and extending the depth of ion implanted region and the damaged layer [18]. The depth of Ar ions distribution corresponds to the depth of the stressed layer induced by Ar ion implantation.

To understand the distribution of Ar ions in implanted fused silica, cross sectional TEM analysis was applied. Fig. 2(a) shows the cross-sectional TEM image in the surface of 10 keV Ar+ implanted into fused silica at a fluence of 1×10^{17} ions/cm^2. As fused silica is amorphous, the interface between implanted area and un-implanted area is not obvious. The yellow dots in the image are Argon bubbles indicating the distribution of implanted Ar+ ions. This image shows the ion-distributed region which goes to a depth of about 50 nm. Argon bubbles are mainly distributed on the surface, and the concentration of Argon bubbles gradually decrease with the increase of depth. The results are in agreement with the calculated results from the TRIDYN simulation and the profilometer measurement, but different from the SRIM calculated results which don't take into account the sputtering effect. For the cross-sectional TEM image, the Argon bubbles are counted and the size distribution of Ar bubbles in fused silica is shown in Fig. 2(b). The size of Argon bubbles ranges from 0.1 to 0.65 nm in diameter. Most Argon bubbles have a diameter of 0.25~0.45 nm. The Argon bubbles distribute in fused silica and lead to a densitified surface.

3.2. Surface morphology and roughness evolution

To investigate the evolution of surface microstructures in Ar-implanted fused silica, the surface morphologies have been characterized using the optical microscopy. The optical micrographs of Ar-implanted fused silica samples at 10 keV with different fluences are shown in Fig. 3. From the graph, the Ar ion implantation shows little influence on the surface morphology of fused silica when the ion fluence is below 1×10^{17} ions/cm^2. The Ar bubbles were observed on the surface of fused silica at an ion fluence of 5×10^{17} ions/cm^2. The amount and size of the Ar bubbles increase with the further increase of ion fluence. This is because that the implanted Ar ions have combined with the vacancy type defects to form Ar-vacancy complexes which have acted as the nucleation centers for bubbles. As the ion fluence increases, the Ar-vacancy complexes further capture more Ar ions and vacancies, and then grow up to form the Ar bubbles [19]. Furthermore, the amount and size of Ar bubbles

generally increase with the increasing fluence, which is probably caused by the increases of lateral stress and gas pressure [20].

To better understand the detailed surface microstructure, the surface morphologies of 10 keV Ar ion-implanted fused silica samples as a function of ion fluence were measured by AFM. The 3D AFM images in 20 μm×20 μm square region of the surface are shown in Fig. 4, and the root mean square (RMS) roughness data of the surfaces were calculated from the AFM measurements and the results are shown in Fig. 5. There are scratches and pits on the un-implanted sample surface and the RMS roughness is 1.084 nm. In the fluence range of $0\sim1\times10^{17}$ ions/cm^2, the surface roughness decreases slightly with the increasing ion fluence, and reaches the minimum value of 0.953 nm at 1×10^{17}ions/cm^2. The sample surface is smooth which may be due to the squeezing action and sputtering effect induced by ion implantation to passivate or remove the surface defects. When the ion fluence exceeds 1×10^{17} ions/cm^2, the defects like bulges and pits appear at the sample surface, and its number and size increase with the increasing ion fluence. Therefore, the surface quality becomes worse and the roughness increases from 1.061 nm at 5×10^{17} ions/cm^2 close to the roughness of the un-implanted sample surface to 2.183 nm at 1×10^{18} ions/cm^2 which is more than twice of the un-implanted one. Clearly the Ar ion implantation has a significant influence on the sample's surface morphology at a high ion fluence, which may be caused by the appearance and expansion of Ar bubbles.

From the results of optical micrographs and AFM images, it can be concluded that Ar ion implantation has little effect on the morphology of fused silica surface at the low ion fluence. With the increasing fluence, the sample surface shows Ar bubbles, as the fluence increases up to 1×10^{18} ions/cm^2, the bubble expansion leads to a much rougher surface with a poor surface quality.

3.3. Defects analysis

To investigate the chemical structure defects of Ar-implanted fused silica with different ion fluences, the PL spectra of all samples were measured and the results are shown in Fig. 6. The PL spectrum of un-implanted sample surface shows several main emission peaks which are attributed to the defects: oxygen deficient center (ODC, 390 and 445 nm), self-trapped exciton (STE, 508 and 573 nm) and non-bridging oxygen hole center (NBOHC, 645 nm) [21]. The emission peak at 320 nm in the PL spectra may be induced by the impurity ions, which needs to be further identified. After ion implantation, there is no new emission peak appeared in the PL spectrum, but the intensities of emission peaks change apparently with the fluences.

With a fluence value of 0~1×10^{17} ions/cm^2, the intensities of all emission peaks dramatically decrease at first, and then the decreasing rate seems to slow down and the intensities reach the weakest value at 1×10^{17} ions/cm^2 where only the ODC (445 nm) defect peak exits in the luminescence spectra. When the fluence is larger than 1×10^{17} ions/cm^2, the intensities of the emission peaks began to increase with the increasing fluence, in especial the intensity of the ODC (445nm) defect peak increases more significantly. The intensity of the emission peak indicates the density of the chemical structure defects. Ion implantation generally results in the breaking of the Si-O bonds and formation of the dangling bonds (e.g., silicon dangling bonds and oxygen dangling bonds) which become the precursors of various defects [22, 23]. Simultaneously the sample will be heated due to ion bombardment, which has a similar effect as to the post-annealing treatment. This results in the recombination of the defects at the sample surface (e.g., recombination of interstitial-elements and vacancy as well as restoration of atomic bonds) [23]. The intensity changes of the emission peaks with the fluence are the result of competition between the formation and recombination of the defects. Our results indicate that a fluence of 1×10^{17} ions/cm^2 might be the optimized ion fluence for this study, because the least concentrations and types of the defects are found at this influence value.

3.4. Evolution of surface molecular structures

To explore the changes of surface molecular structures induced by Ar ion implantation, the infrared absorption spectra of both un-implanted and Ar-implanted fused silica samples with different fluences were measured and the results are shown in Fig. 7 for comparisons. All the spectra have two broad absorption peaks in the range of 630~860 cm^{-1} and 860~1270 cm^{-1}, which can be fitted with four Gaussian absorption components peaked at about 783.7, 955.1, 1044.1 and 1179.6 cm^{-1}, corresponding to Si-O-Si bending vibration (TO_2), Si-OH bridging (υ_1), transverse optical (TO_3) and longitudinal optical (LO_3) components for Si-O-Si asymmetric stretching vibrations, respectively [23, 24]. The Gaussian components of infrared absorption spectra for un-implanted and ion-implanted samples are shown in Fig. 8, and the corresponding Gaussian bands are listed in Table 2. Based on the above measurement results, the shift of peak positions of the infrared absorption spectra indicates that the surface molecular structures have been changed during the Ar ion implantation process. The fundamental Si-O-Si stretching band is the predominant structural band in the infrared absorption spectra, which is commonly used to monitor changes of the Si-O-Si bond angles for the fused silica [25]. For ion-implanted samples, there is a shift of Si-O-Si stretching band

towards the lower frequency side, indicating that the Si-O-Si bond angle decreases and the density of the fused silica surface increases. This means that the ion implantation into fused silica causes densification of the structure. The density of the fused silica can be calculated by the Fictive temperature which is determined by the peak position of Si-O-Si stretching band. When fused silica is cooled rapidly from a high temperature molten state, the sub-equilibrium structure will be frozen and the corresponding high temperature is called fictive temperature. The relation between the fictive temperature of fused silica and the glass density has been reported and is generally written using the following equation [26]:

$$\rho(\mathrm{g/cm^3})=9.39\times10\text{-}6T_f(^{\circ}\mathrm{C})+2.1902 \quad (1)$$

where，ρ and T_f are the density and the fictive temperature of fused silica, respectively.The peak position of the overtone for the Si-O-Si asymmetric stretching vibration in the infrared transmission spectrum is commonly used to determining the fictive temperature of the fused silica, and the relationship between the peak position and the corresponding fictive temperature from 1000 ℃ to 1550 ℃ has been established as [27]:

$$\upsilon_{\mathrm{p}} = 2221.2 + 6.1086(\frac{10^4}{T_f}) - 0.097385(\frac{10^4}{T_f})^2 \quad (2)$$

where, υ_{p} is the peak position of the overtone for the Si-O-Si asymmetric stretching vibration in infrared transmission spectrum at around 2260 $\mathrm{cm^{-1}}$. According to the linear relationship [28], the relation of the peak position of the overtone for the asymmetric stretching vibration to the peak position of the TO_3 asymmetric stretching vibration can be written as:

$$\upsilon_{\mathrm{p}}=1376.8+0.8544\upsilon_{\mathrm{TO3}} \quad (3)$$

where, υ_{TO3} is the peak position of the TO_3 asymmetric stretching vibration of Si-O-Si bridge in infrared absorption spectra.

Based on the formula (1), (2) and (3), the fictive temperature and the density of both un-implanted and ion-implanted sample surfaces can be obtained and summarized in Table 2. The results show that the density of fused silica surface increases with the increasing fluence and reaches the maximum value of 2.2026 $\mathrm{g/cm^3}$ at $1\times10^{17}\mathrm{ions/cm^2}$, then gradually decreases to 2.2007 $\mathrm{g/cm^3}$ at 1×10^{18} $\mathrm{ions/cm^2}$, which is still larger than the density of un-implanted sample surface. Ion implantation leads to the densification of fused silica surface, but too large a fluence will cause the sample surface to swell, thus the density decreases. The change of the sample surface density with the fluence is consistent with the fictive temperature, which is opposite to the changes of Si-O-Si bond angle and the shift of the Si-O-Si stretching band.

3.5. Mechanical properties characterization

Ion implantation has a significant influence on the mechanical properties of sample, including residual stress, hardness and elastic modulus. Generally the ion implantation layer has a scale which is about micrometer or submicrometer thick. Therefore, nanoindentation technique is ideal for studying the properties of relatively thin modified surface layer because of its ability to apply small controlled force and measure small displacement.

The residual stress on the sample surface can be estimated by comparing the load-depth curves of the stress-free surface and the stressed surface. At the fixed load, the loading/unloading curves under the compressive stress generally shift to left, whereas it would be the opposite direction under the tensile stress. The shift of the loading/unloading curves increases with the increasing residual stress [29]. For the samples before and after Ar ion implantation, the load-depth curves at different maximum loading force (F_{max}) are shown in Fig. 9. It can be seen that a compressive stress was induced by Ar ion implantation at the depth range of 0 to 60 nm in Fig. 9(a), because the depth of indenter penetrating into ion-implanted surface decreases at the fixed loading force, indicating that the loading/unloading curves shift to the left. The compressive stress of sample surface increases firstly with the increase of the ion fluence, reaches the maximum at 1×10^{17} ions/cm^2, and then decreases slightly with the further increase of the fluence. This is consistent with the changing trend of sample‘s density measurement results. The results indicate that the compressive stress might be resulted from the surface densification. As the maximum loading force increases, the shift of the loading/unloading curves of ion-implanted surface compared to the un-implanted one gradually decreases and finally there is no difference under a very large loading force. This indicates that the compressive stress exists mainly in the top surface layer, which is about dozens of nanometers for the 10 keV Ar-implanted fused silica.

Based on the load-depth curves of un-implanted and Ar-implanted fused silica samples, the hardness (H) and elastic modulus (E) at different fluences for each fixed maximum loading force were obtained based on the Oliver and Pharr method [30]. The results are listed in Table 3. It can be seen the hardness and elastic modulus increase at moderate fluences. This is mainly caused by the compressive stress at the surface and densification effect. When the F_{max} was 0.5 mN (final depth, d< 60nm), the hardness value is small known as the reverse indentation size effect, which is caused by numerous reasons including the pile-up or send in effect, the geometry of the indenter tip, and the sample surface [31, 32]. This value is smaller than the value ~10 GPa, which is the bulk hardness when the maximum loading force is more

than 1 mN (final depth, d> 75 nm). Based on the above results, Ar ion implantation at fluence of 1×10^{17} ions/cm^2 will form large compressive stress on the sample surface to improve the mechanical properties of fused silica effectively.

3.6. Damage performance measurement

To investigate the laser damage behavior of Ar-implanted fused silica with different fluences, twenty points were selected randomly to calculate the average LIDT for each sample to minimize the meansurement error induced by the stability of laser, the change of surrounding environment and the difference between samples. The results are shown in Fig. 10. The LIDT of un-implanted sample is 15.12 J/cm^2 and the LIDTs of implanted samples are 18.16 J/cm^2, 17.88 J/cm^2 and 19.33 J/cm^2 at the fluences of 1×10^{16} ions/cm^2, 5×10^{16} ions/cm^2 and 1×10^{17} ions/cm^2, with an enhancement ratio of 20.11 %, 18.25 % and 27.84 %, respectively. The results indicate that the LIDT of fused silica is improved by Ar ion implantation at fluence range of 1×10^{16} ions/cm^2~ 1×10^{17} ions/cm^2. This phenomenon can be explained by the fact of the recombination of the chemical defects (ODC, NBOHC, STE, etc.), surface densification and the compressive stress formed on the sample surface, and thus a significant strengthening effect on the sample surface. However, when the ion fluence is too large, the laser damage threshold will decrease, which is due to the formation of rough surface with Ar bubbles and the increase of the densities of the chemical structure defects, especially for the existence of ODC (445 nm) defects. At the fluence of 5×10^{17} ions/cm^2, there is no obvious improvement in laser damage threshold. When the ion fluence is up to 1×10^{18} ions/cm^2, the LIDT of fused silica sample is reduced to 14.49 J/cm^2 which is even lower than that of the un-implanted sample. Therefore, Ar ion implantation can improve the LIDT of fused silica with the optimized fluence range of 1×10^{16} ions/cm^2~1×10^{17} ions/cm^2 in this work.

4. Conclusions

Ar ions of 10 keV at different fluences have been implanted into fused silica samples. Surface morphology, optical and mechanical properties, as well as LIDTs were investigated. The results indicate that the surface morphology has no apparent changes at a low fluence, but distinctly changes when the fluence exceeds 1×10^{17} ions/cm^2, which is mainly caused by formation of Ar bubbles. The concentration of chemical structure defects decreases firstly and then increases with the increasing fluence, and this is dependent on the competition between the formation and recombination of the defects. Ar ion implantation leads to the reduction of Si-O-Si bond angle, surface densification and generation of compressive stress

layer, thus strengthening the surface of fused silica. The LIDT test results demonstrated that the surface quality, chemical structure defects and compressive stress have important influences on the laser damage performance of Ar-implanted fused silica. Based on the LIDT data, an ion flunece range of 1×10^{16} ions/cm^2~1×10^{17} ions/cm^2 was found to be the preferable parameters to improve the LIDT of fused silica under Ar ion implantation.

Acknowledgments

This work is financially supported by the Key Project of National Natural Science Foundation of China-China Academy of Engineering Physics joint Foundation (NSAF, Grant No. U1830204). The authors would like to thank Prof. Wolfhard Möller and Dr. Roman Böttger from the Institute of Ion Beam Physics and Materials Research, Helmholtz-Zentrum Dresden-Rossendorf, Germany, for providing the latest version of the TRIDYN simulation code. The authors would also like to thank Dr. Hiro Amekura in the Institute of Research Center for Advance Measurement and Characterization, National Institute for Materials Science, Japan, for providing help and useful suggestions and discussion.

References

[1] R.A. Hawleyfedder, C.J. Stolz, J.A. Menapace, M.R. Borden, J. Yu, M.J. Runkel, M.D. Feit, NIF optical materials and fabrication technologies: an overview, Proc. SPIE 5341 (2004) 102-105.

[2] M.D. Feit, F.Y. Genin, A.M. Rubenchik, L.M. Sheehan, S. Schwartz, M.R. Kozlowski, J. Dijon, P. Garrec, J. Hue, Statistical description of laser damage initiation in NIF and LMJ Optics at 355 nm, Proc. SPIE 3492 (1999) 188-195.

[3] H.S. Peng, X.F. Wei, F. Jing, D.Y. Fan, J. Zhou, Design of 60-kJ SG-III laser facility and related technology development, Proc. SPIE 4424 (2001) 98-103.

[4] M.L. Spaeth, P.J. Wegner, T.I. Suratwala, M.C. Nostrand, J.D. Bude, A.D. Conder, J.A. Folta, J.E. Heebner, L.M. Kegelmeyer, B.J. Macgowan, Optics Recycle Loop Strategy for NIF Operations above UV Laser-Induced Damage Threshold, Fusion Sci. Technol. 69 (2016) 265-294.

[5] L.W. Hrubesh, M.A. Norton, W.A. Molander, E.E. Donohue, S.M. Maricle, B. Penetrante, R.M. Brusasco, W. Grundler, J.A. Butler, J. Carr, Methods for mitigating surface damage growth in NIF final optics, in: Boulder Damage, 2002, pp. 23-33.

[6] Z. Zheng, X.T. Zu, X.D Jiang, X. Xiang, J. Huang, X.D. Zhou, C.H. Li, W.G. Zheng, L. Li, Effect of HF etching on the surface quality and laser-induced damage of fused silica, Opt. Laser Technol. 44 (2012) 1039-1042.

[7] Y. Jiang, X. Xiang, C.M. Liu, H.J. Wang, W. Liao, H.B. Lv, X.D. Yuan, R. Qiu, Y.J. Yang, W.G. Zheng, X.T. Zu, Effect of residual stress on laser-induced damage characterization of mitigated damage sites in fused silica, J. Non-Cryst. Solids 410 (2015) 88-95.

[8] Y. Jiang, X. Xiang, X.D. Yuan, C.M. Liu, H.J. Wang, C.S. Luo, S.B. He, H.B. Lv, W.G. Zheng, X.T. Zu, Characterization of 355 nm laser-induced damage of mitigated damage sites in fused silica, Laser Phys. 23 (2012) 54-58.

[9] F. Dahmani, J.C. Lambropoulos, A.W. Schmid, S. Papernov, S.J. Burns, Crack arrest and stress dependence of laser-induced surface damage in fused-silica and borosilicate glass, App. Opt. 38 (1999) 6892-6903.

[10] A. Kusov, A. Kondyrev, A. Chmel, Common approach to the problem of defect nucleation in solids under 'pre-threshold' laser irradiation, J. Phys.: Condens. Matter. 2 (1990) 4067-4080.

[11] T.E. Felter, L. Hrubesh, A. Kubota, L. Davila, M. Caturla, Laser damage probability studies of fused silica modified by MeV ion implantation, Nucl. Instr. and Meth. in Phys. Res. B 207 (2003) 72-79.

[12] M.L. Brongersma, E. Snoeks, T.V. Dillen, A. Polman, Origin of MeV ion irradiation-induced stress changes in SiO_2, J. Appl. Phys. 88 (2000) 59-64.

[13] N. Kalyanasundaram, M.C. Moore, J.B. Freund, H.T. Johnson, Stress evolution due to medium-energy ion bombardment of silicon, Acta. Mater. 54 (2006) 483-491.

[14] M.L. Brongersma, E. Snoeks, A. Polman, Temperature dependence of MeV heavy ion irradiation-induced viscous flow in SiO_2, Appl. Phys. Lett. 71 (1997) 1628-1630.

[15] J.F. Ziegler, The Stopping and Range of Ions in Solids, Ion Implantation Science & Technology 10 (1984) 51-108.

[16] W. Riede, D. Ristau, Laser-induced damage measurements according to ISO/DIS 11 254-1: results of a national round robin experiment on Nd:YAG laser optics, Proc. SPIE 3244 (1997) 96-105.

[17] N.L. Anderson, R.P. Vedula, P.A. Schultz, R.M. Van Ginhoven, A. Strachan, First-principles investigation of low energy E' center precursors in amorphous silica, Phys. Rev. Lett. 106 (2011) 206402-206405.

[18] I.O. Usov, S. Rubanov, J. Won, A.A. Suvorova, Transformation of YSZ under high fluence argon ion implantation, Nucl. Instr. and Meth. in Phys. Res. B 326 (2014) 283-288.

[19] V. Raineri, M. Saggio, E. Rimini, Voids in silicon by He implantation: From basic to applications, J. Mater. Res. 15 (2000) 1449-1477.

[20] W. Primak, Radiation blistering: interferometric and microscopic observations of oxides, silicon and metals, J. Appl. Phys. 37 (1966) 2287-2294.

[21] M.A. Stevens-Kalceff, J. Wong, Distribution of defects induced in fused silica by ultraviolet laser pulses before and after treatment with a CO_2 laser, J. Appl. Phys. 97 (2005) 113519-113511-113518.

[22] L. Skuja, M. Hirano, H. Hosono, K. Kajihara, Defects in oxide glasses, Phys. Stat. Sol(c) 2 (2005) 15–24.

[23] B. Garrido, J. Samitier, S. Bota, C. Domínguez, J. Montserrat, J.R. Morante, Structural damage and defects created in SiO_2 films by Ar ion implantation, J. Non-Cryst. Solids 187 (1995) 101-105.

[24] M. Tomozawa, J.W. Hong, S.R. Ryu, Infrared (IR) investigation of the structural changes of silica glasses with fictive temperature, J. Non-Cryst. Solids 351 (2005) 1054-1060.

[25] A. Agarwal, Correlation of silica glass properties with the infrared spectra, Chin. J. Catal. 35 (1997) 120–126.

[26] J.E. Shelby, Density of vitreous silica, J. Non-Cryst. Solids 349 (2004) 331-336.

[27] H. Kakiuchida, K. Saito, A.J. Ikushima, Precise Determination of Fictive Temperature of Silica Glass by Infrared Absorption Spectrum, J. Appl. Phys. 93 (2003) 777-779.

[28] A. Agarwal, K.M. Davis, M. Tomozawa, A simple IR spectroscopic method for determining fictive temperature of silica glasses, J. Non-Cryst. Solids 185 (1995) 191-198.

[29] Y.H. Lee, D. Kwon, Measurement of residual-stress effect by nanoindentation on elastically strained (100 ja:math) W, Scripta Mater. 49 (2003) 459-465.

[30] Oliver, W.C, Pharr, G.M, An improved technique for determining hardness and elastic modulus using load and displacement sensing indentation experiments, J. Mater. Res. 7 (1992) 1564-1583.

[31] O. Sahin, O. Uzun, U. Lolenen, B. Duzgun, N. Ucar, Indentation Size Effect and Microhardness Study of β-Sn Single Crystals, Chin. Phys. Lett. 22 (2005) 3137-3140.

[32] M. Li, W.M. Chen, Factors resulting in micron indentation hardness descending in indentationtests, Chin. J. Aeronaut. 22 (2009) 43-48.

Table 1 Simulation parameters for SRIM.

Atoms	Density (g/cm^3)	Displacement energy (eV)	Lattice binding energy (eV)	Surface binding energy (eV)
Si	2.2	15	2	4.7
O		28	3	2

Table 2 Peak positions of the infrared absorption spectra and densities of sample surfaces before and after implantation.

Fluence	Group vibration model				Fictive	Density
(ions/cm^2)	TO_2 (cm^{-1})	υ_1 (cm^{-1})	TO_3 (cm^{-1})	LO_3 (cm^{-1})	temperature (°C)	(g/cm^3)
0	783.7	955.1	1044.1	1180.7	1094.0	2.2005
1×10^{16}	783.4	953.4	1041.6	1179.2	1154.6	2.2010
5×10^{16}	783.0	950.6	1036.9	1176.9	1286.4	2.2023
1×10^{17}	783.6	951.1	1035.8	1176.3	1323.3	2.2026
5×10^{17}	783.5	950.4	1037.2	1176.6	1279.3	2.2022
1×10^{18}	783.4	954.2	1043.3	1179.6	1113.6	2.2007

Table 3 Hardness, elastic modulus and final penetrated depth of Ar-implanted fused silica surfaces with different fluences at fixed maximum loading force.

		Ar ion fluence (ions/cm^2)			
		0	1×10^{16}	1×10^{17}	1×10^{18}
F_{max}=0.5 mN	Hardness, *H* (GPa)	9.097	9.784	9.850	9.054
	Elastic modulus, *E* (GPa)	74.389	73.953	76.931	73.277
	Final depth, *d* (nm)	58.180	54.609	47.455	50.376
F_{max}=1 mN	Hardness, *H* (GPa)	10.216	10.235	10.497	10.118
	Elastic modulus, *E* (GPa)	76.638	76.300	78.661	78.040
	Final depth, *d* (nm)	75.306	73.536	72.005	73.003
F_{max}=5 mN	Hardness, *H* (GPa)	10.226	10.392	10.535	10.409
	Elastic modulus, *E* (GPa)	75.053	76.703	78.410	76.811
	Final depth, *d* (nm)	188.170	184.435	180.677	184.096
F_{max}=15 mN	Hardness, *H* (GPa)	10.219	10.133	10.238	10.287
	Elastic modulus, *E* (GPa)	75.303	76.705	76.800	76.032
	Final depth, *d* (nm)	338.747	337.810	333.703	336.080

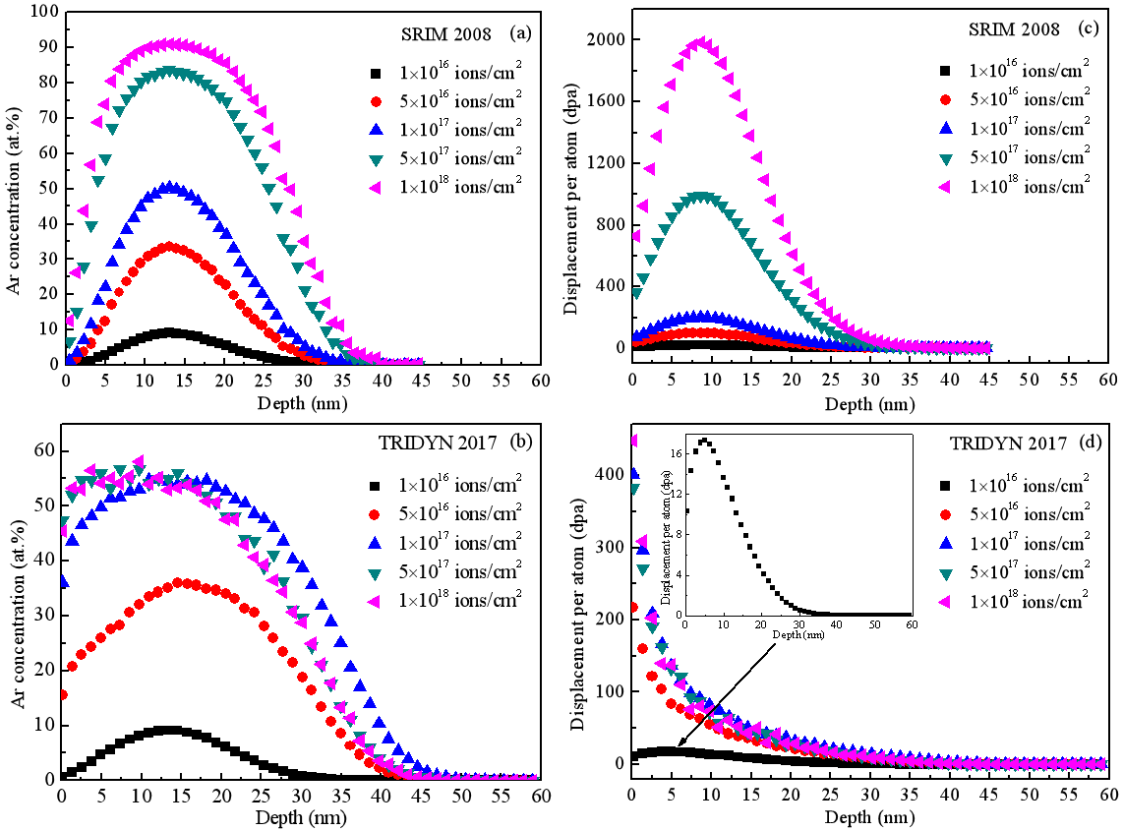

Fig. 1. SRIM and TRIDYN calculations of 10 keV Ar-implanted fused silica with different fluences: Ar ion concentration (a, b) and dpa (c, d) distributions.

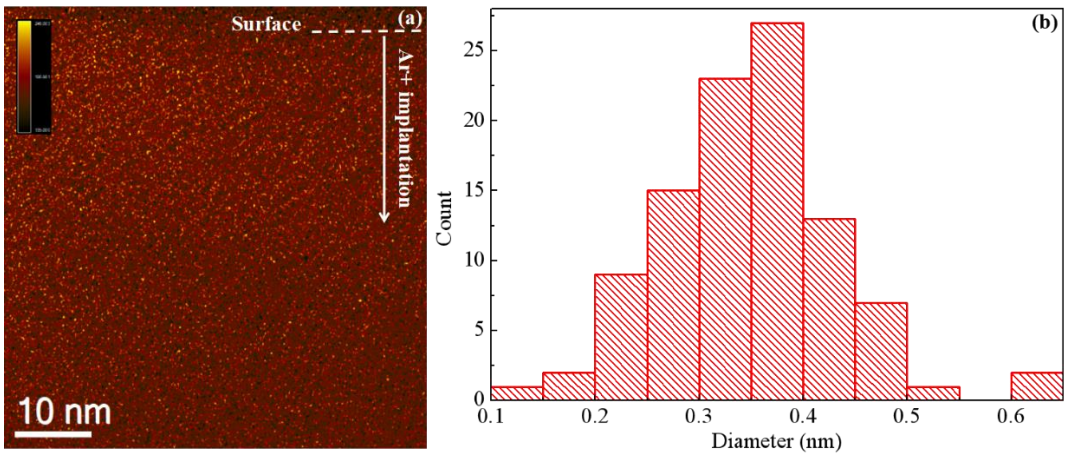

Fig. 2. Cross-sectional TEM image (a) and Argon bubble size distribution (b) of 10 keV Ar+ implanted fused silica at fluence of 1×10^{17} ions/cm^2.

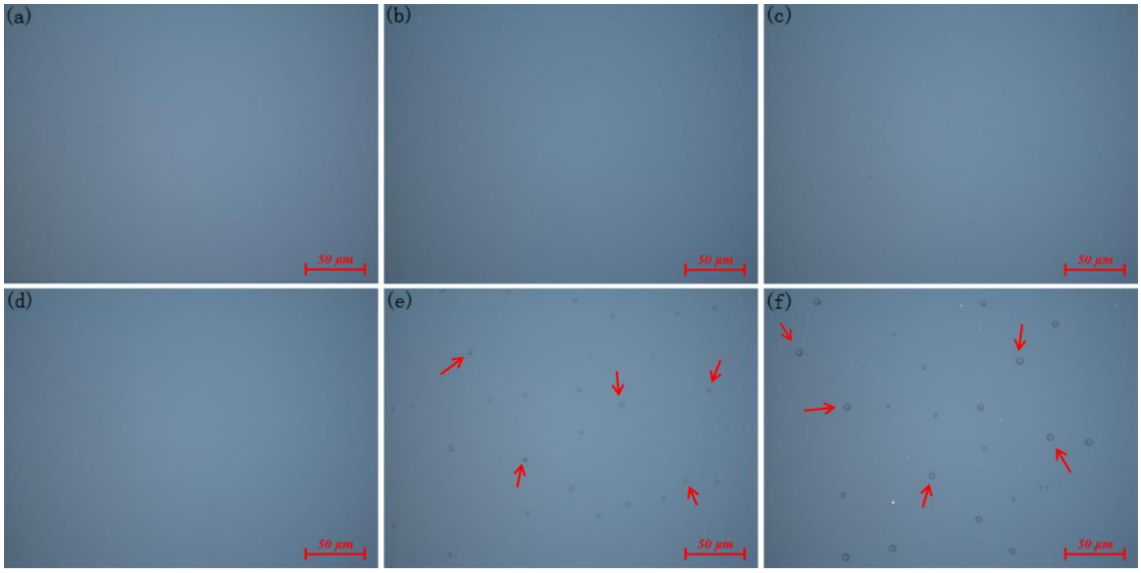

Fig. 3. Optical micrographs of Ar-implanted fused silica samples with different fluences: (a) 0; (b) 1×10^{16}; (c) 5×10^{16}; (d) 1×10^{17}; (e) 5×10^{17}; (f) 1×10^{18} ions/cm^2.

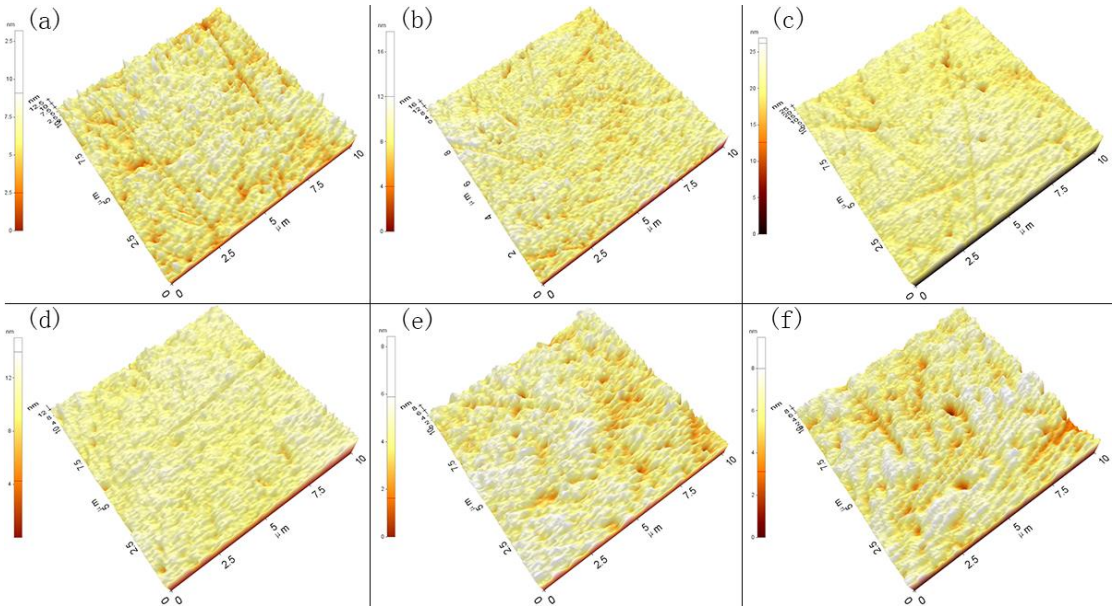

Fig. 4. AFM images of Ar-implanted fused silica samples with different fluences: (a) 0; (b) 1×10^{16}; (c) 5×10^{16}; (d) 1×10^{17}; (e) 5×10^{17}; (f) 1×10^{18} ions/cm^2.

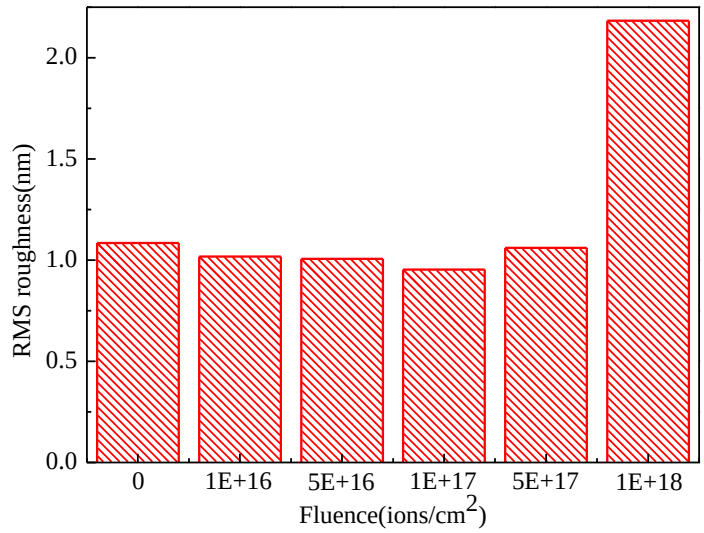

Fig. 5. Surface RMS roughness as a function of the fluence.

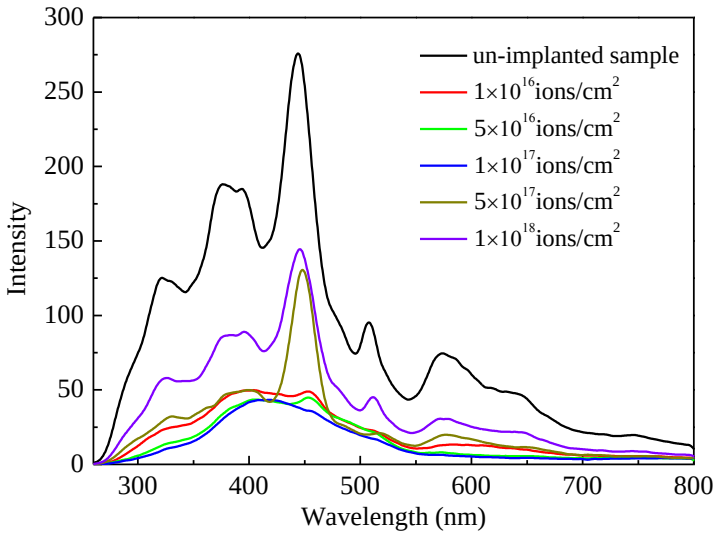

Fig. 6. Photoluminescence spectra of Ar-implanted fused silica with different fluences.

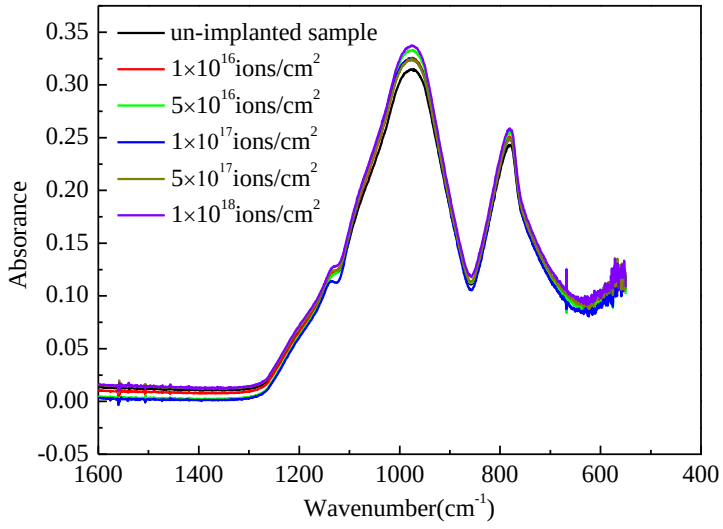

Fig. 7. Infrared absorption spectra of Ar-implanted fused silica with different fluences.

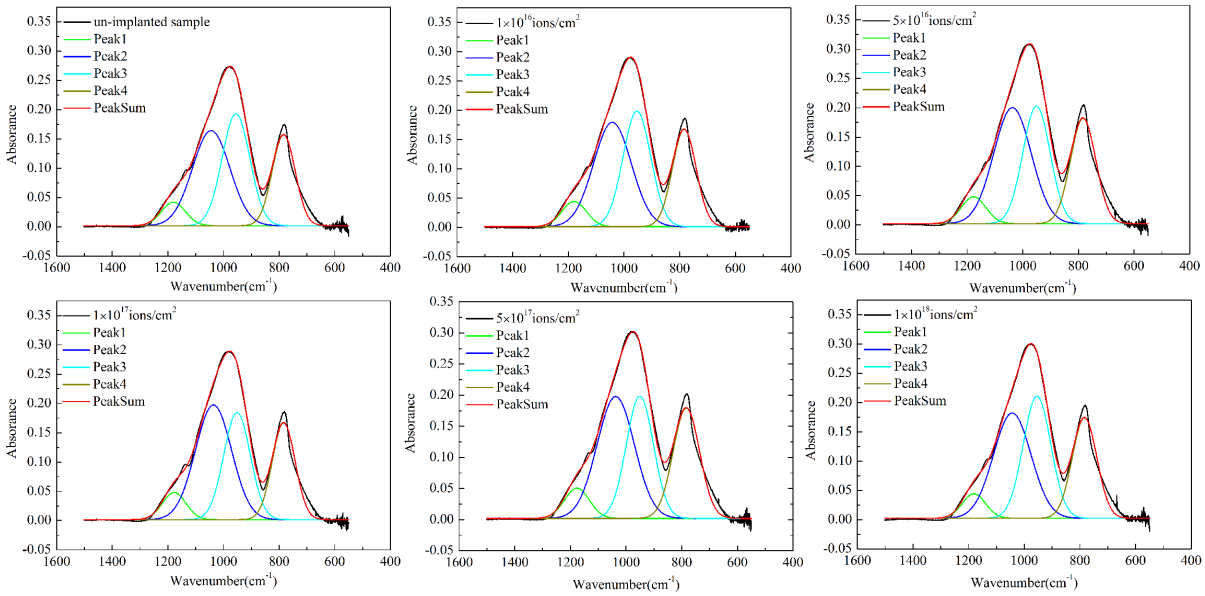

Fig. 8. Gaussian components of infrared absorption spectra for un-implanted and ion-implanted samples.

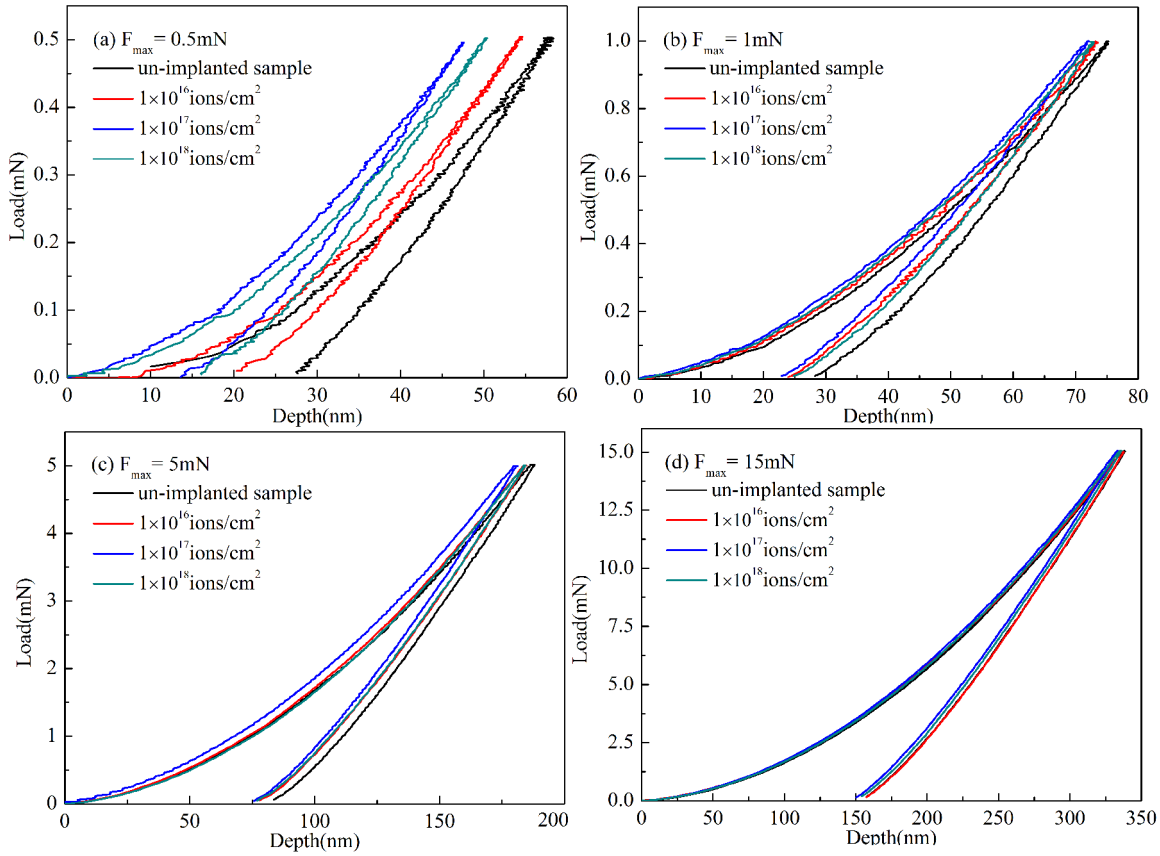

Fig. 9. Load-depth curves of Ar-implanted fused silica with different fluences at fixed maximumloading force: (a) 0.5, (b) 1, (c) 5, (d) 15 mN.

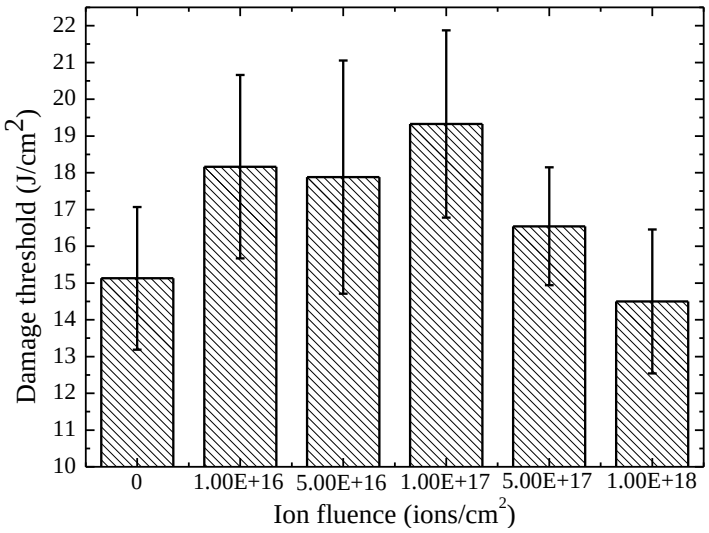

Fig. 10. LIDTs of Ar-implanted fused silica samples with different fluences.